# Systematic study of the hybrid plasmonic-photonic band structure underlying lasing action of diffractive plasmon particle lattices

A. Hinke Schokker,[1] Floor van Riggelen,[1] Yakir Hadad,[2,*] Andrea Alù,[2,1] and A. Femius Koenderink[1,†]

[1]*Center for Nanophotonics, AMOLF, Science Park 104, 1098 XG Amsterdam, The Netherlands*

[2]*Department of Electrical and Computer Engineering, The University of Texas at Austin, 1616 Guadalupe Street, UTA 7.215, Austin, Texas 78712, USA*

(Received 7 June 2016; revised manuscript received 13 January 2017; published 8 February 2017)

We study lasing in distributed feedback lasers made from square lattices of silver particles in a dye-doped waveguide. We present a systematic analysis and experimental study of the band structure underlying the lasing process as a function of the detuning between the particle plasmon resonance and the lattice Bragg diffraction condition. To this end, as gain medium we use either a polymer doped with Rh6G only, or polymer doped with a pair of dyes (Rh6G and Rh700) that act as a Förster energy transfer (FRET) pair. This allows for gain, respectively, at 590 or 700 nm when pumped at 532 nm, compatible with the achievable size tunability of silver particles embedded in the polymer. By polarization-resolved spectroscopic Fourier microscopy, we are able to observe the plasmonic/photonic band structure of the array, unraveling both the stop gap width, as well as the loss properties of the four involved bands at fixed lattice Bragg diffraction condition and as a function of detuning of the plasmon resonance. To explain the measurements we derive an analytical model that sheds insights on the lasing process in plasmonic lattices, highlighting the interaction between two competing resonant processes, one localized at the particle level around the plasmon resonance, and one distributed across the lattice. Both are shown to contribute to the lasing threshold and the overall emission properties of the array.

DOI: 10.1103/PhysRevB.95.085409

## I. INTRODUCTION

Organic distributed feedback lasers have been widely studied since the mid-1990s for their ability to provide large area lasing upon optical or electrical pumping, while being very simple to fabricate [1]. Such lasers generally consist of an organic gain medium that is deposited as a thin layer over a periodically corrugated dielectric surface, with a periodicity chosen such that it offers an in-plane Bragg diffraction condition within the gain window [2,3]. A wide range of emission wavelengths can be selected through the availability of a vast variety of organic fluorophores and fluorescent polymers, while the typically small corrugations over the surface can be realized through optical lithography, or soft imprint lithography [4,5].

More recently a different class of lasers was proposed that rely on plasmonic effects. Plasmonics uses the fact that free electrons in metals offer a collective resonance at optical frequencies [6]. This causes metal nanoparticles or nanostructured surfaces to provide highly enhanced and strongly localized electromagnetic fields upon irradiation, boosting the spontaneous emission rate of coupled fluorescent emitters [7–9]. When such plasmonic particles are placed in two-dimensional diffractive periodic arrays, they can also provide control over emission directivity and brightness, due to the hybridization of localized plasmonic resonances with grating anomalies associated with the array geometry and surrounding dielectric environment [10–12]. In particular, these systems have been studied as substrates for surface enhanced Raman scattering (SERS) [13], sensing [14,15], and solid-state lighting [10,16]. Recently, several groups [17–20] have shown distributed feedback lasing in such plasmonic periodic systems. A significant difference with conventional distributed feedback lasers is that, while the dielectric perturbation is typically weak and nonresonant, for plasmonic systems the scattering strength per unit cell of the lattice can become very strong, and strongly dispersive, around the supported resonance. One practical advantage is that strong scattering implies broader stop gaps, which corresponds to smaller Bragg scattering lengths, or equivalently much smaller required device sizes for lasing, and large robustness to disorder [21].

In earlier work [20], some of us presented an experimental observation of the plasmonic band structure underlying lasing action of a plasmon particle lattice coupled to a dielectric waveguide that also provides gain. In this system Bragg resonance was established using diffraction by metal particles which are relatively strong scatterers compare to all-dielectric gratings. However, in that study the plasmonic particles were off resonance within the gain window and the lasing frequency set by the lattice periodicity. Therefore their individual scattering, while stronger than that of dielectric corrugations, was still weak compared to the maximum attainable cross section. Likewise, in work by other groups [17–19] on lasing in systems with surface lattice resonances (diffractive plasmonic resonances without assistance of a waveguide mode), the plasmon particle resonance frequency was not systematically varied. On the contrary, here we present a systematic study of the band structure underlying lasing when the plasmon resonance is tuned close to, and onto, the lasing condition. We identify a systematic dependence of the stop gap width on the scattering strength of the particles. Moreover, we find that, as the plasmon resonance crosses the lasing condition, the loss characteristics of the supported bands interchange and, as a consequence, also the stop gap edge at which lasing occurs moves from the low to the high end of the gap.

[*]Present address: School of Electrical Engineering, Tel-Aviv University, Tel-Aviv, Israel, 69978.

[†]f.koenderink@amolf.nl

 

These findings are in full agreement with an electrodynamic point dipole analytical model that we develop in this work, accounting for near- as well as far-field interactions among the particles mediated by the waveguide structure in which they are deposited. This paper is structured as follows. In Secs. II and III we develop and analyze a rigorous theoretical study of the structure's complex-valued dispersion relation based on this dipolar model. In Secs. IV and V we introduce our experimental methods and report on the spectroscopy of our gain medium. In Secs. VI and VII we analyze band structure measurements, showing that they validate our theory for the competing resonant phenomena behind the lasing effect. We close by a real-space full-wave analysis in Sec. IX.

## II. SEMIANALYTICAL MODEL

In this section we theoretically analyze the mode structure of two-dimensional plasmon particle lattices embedded in planar waveguides using the discrete dipole approximation. The geometry of interest is an infinite square lattice of silver cylindrical particles with periodicity $d$ embedded in a high index slab that acts as waveguide and through doping also acts as gain medium [Fig. 1(a)]. Commensurate with the experiments reported here and in Ref. [20], we take this slab to have a thickness $h = 450$ nm and relative dielectric constant $\epsilon_2 = 2.79$ (equivalent to the polymer SU8). The slab is surrounded by air on one side ($\epsilon_1 = 1$, located at $z > h$), and glass on the other (substrate with $\epsilon_3 = 2.25$ located at $z < 0$). The array is embedded close to the SU8-glass interface, as shown in Fig. 1. The air/SU8/glass stack supports a single transverse electric (TE) and a single transverse magnetic (TM) mode of almost identical mode index (1.55, calculated using the method of Urbach and Rikken [22]). Mode profiles [Figs. 1(c) and 1(d)] evidence that the TE mode has a strong polarization component in the plane in which the particles are polarizable, while the TM mode has only weak overlap. To understand the physics of the particles' interaction with the modes, we have conducted FDTD simulations (Lumerical, using tabulated optical constants [23]) to determine extinction cross sections of single particles in the stratified system (incidence from the glass side). As the particle diameter $D = 2r$ increases, the extinction cross section [Fig. 1(b)] strongly increases, and furthermore exhibits the well-known shift to longer wavelengths due to dynamic depolarization effects [24–26]. For $D > 60$ nm, the dipolar resonance has a distinct Lorentzian shape, and is well separated from the features at wavelengths $\lambda < 500$ nm, that are due to intraband features in the dielectric constant.

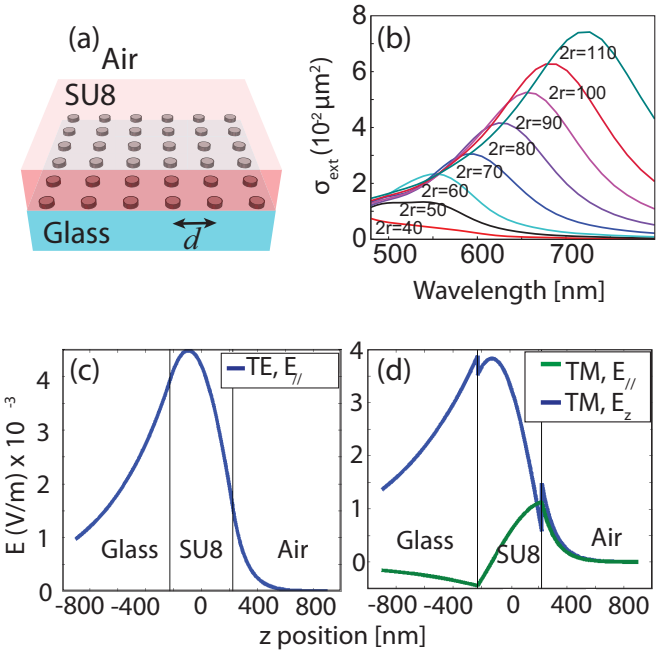


FIG. 1. (a) Schematic of the sample geometry, consisting of a periodic square lattice of thin silver disks (pitch $d$) on a glass substrate, embedded in a high index polymer SU8 that supports a waveguide mode and is doped with organic dye to provide gain. (b) Extinction cross section according to FDTD simulations (Lumerical using CRC tabulated optical constants) of single silver disks of various radii $r$ embedded in the air/SU8/glass system, under normal incidence from the glass side. (c) and (d) Electric field profile of the single TE and single TM mode supported by the structure. In (c) the in-plane field is perpendicular to the in-plane wave vector, while in (d) it is alongside it.

Our goal is to calculate the passive array dispersion of the composite system including loss, as well as the relation between the local surface plasmon resonance excitation strength of the array and the efficiency of coupling to far-field radiation. Since Ohmic and radiation loss are important we target a complex-valued dispersion relation, where the imaginary part of wave number quantifies loss. Lasing is established by a combination of feedback and amplification processes. Particularly, in distributed feedback lasers the former is achieved by a distributed backward Bragg resonance, a result of coupling between counterpropagating slab modes [1]. The threshold for lasing is determined by the quality factor of the feedback mechanism in the absence of gain. Therefore, dominant lasing will take place in the frequency range for which the quality factor of the feedback mechanism is the highest, namely the frequency regions where the imaginary part of the complex dispersion wave number of the resulting coupled slab modes, in the absence of gain, is minimal. At the same time, to observe lasing the emission must be able to couple out into the far field. Our aim is hence to isolate the low-loss points of the complex-valued dispersion diagram that at the same time are not forbidden from coupling to radiation. Since this type of passive-system model accounts for linear loss, but not gain dynamics or spontaneous emission noise, it only gives insight up to threshold, answering what modes will lase first, but not what their nonlinear physics will be well above threshold.

In order to rigorously tackle the above threshold dynamics, one may apply a time-domain approach, such as the finite difference time domain method, which can be used to calculate the real-space field distribution, which is mutually and nonlinearly affected by the four-level system describing the medium through a simultaneous solution of the time-dependent Maxwell equations and the active medium rate equations [27]. Unfortunately, such an approach is limited to finite structures and thereby cannot provide the complex $k$-vector details that naturally emerge in our linear $k$-vector

analysis. Full wave solution methods with periodic boundary conditions naturally deal with infinite systems. However, the Bloch-Floquet boundary condition imposes the wave vector, as opposed to the physics of a lasing process that selects the wave vector. With such real-space methods one can in principle sample $k$ space to map out dispersion and loss, by doing many simulations that sample $k$ space point by point. This approach is limited to real wave vectors and requires significant computational effort. An alternative approach is proposed in [28], where the discrete dipole method is used in the frequency domain, but with the Green's function of an infinite homogeneous medium (therefore no slab modes are considered). In order to obtain a time-domain model that includes the four-level system dynamics, the periodic system response, i.e., the dipole lattice sum, is approximated using the assumptions that (a) the lattice response at diffraction resonance is a Lorentzian single resonance, and (b) that lasing occurs at $k = 0$. Hence, although this analysis captures interesting features of the lasing process above threshold, it does not treat the lasing as a process that originates from noise and settles at the minimal loss $k(\omega)$ points. Using our linear model we find, in accord with our measured data, that not only that lasing takes place at $k \neq 0$ but also that under certain conditions, that are discussed below, there are two rather than one lasing points $k(\omega)$. Therefore we believe that a complete picture of the lasing process in plasmonic array systems requires various complementary perspectives. On the one hand this includes the models proposed in [27–29] for the nonlinear above-threshold regime. As demonstrated in this paper, linear $k$-space modeling provides complementary insight valid up to threshold. Linear $k$-space modeling fully accounts for the loss mechanisms and hence explains the lasing condition that arises from the tradeoff between gain and loss.

As method of choice for our work we focus on a semi-analytical model that describes the particles as strong dipolar scatterers, and accounts for all the electrodynamic multiple scattering interactions in the lattice that may take place via the waveguide. Such electrodynamic point dipole models for lattices have been considered in earlier work mainly in the context of lattices in a homogeneous background [30–33], with a few exceptions that consider also the presence of a dielectric slab [34,35]. It is important to distinguish this method from coupled mode theory typically used for conventional periodically corrugated dielectric waveguides [36]. In solid-state terms, such plane wave expansion methods are equivalent to a "nearly free-photon" approach, where the waveguide dispersion relation folds at the edges of the Brillouin zone, and where the small index contrast causes minute stop gaps to open up. This type of model is not applicable for the case at hand, since the plasmonic particles are characterized by strong individual scattering, which does not perturb, but instead significantly modifies the band structure. This is also evident in numerical plane wave expansion approaches to periodic plasmon particle systems that either do not converge or need of order $10^3$ plane waves to resolve the plasmon particle resonance despite the fact that at the operation point (second order Bragg diffraction) only four diffraction orders couple. Since the plasmonic particles are designed to operate around their dominant dipolar resonance, we have a strong basis to assume that the particle's interaction is essentially dipolar. For this reason, our analytical approach employs an electrodynamic dipole model with Ewald summation to deal with all the retarded dipole-dipole interactions mediated by the waveguide slab. This model builds on recent implementations of periodic point-dipole lattice models that successfully describe the hybridization of localized plasmons with propagating and evanescent photonic diffraction orders [31–33,37–42].

The dipolar response of a scatterer is described by its polarizability response $\alpha(\omega)$, which for a resonant scatterer in the quasistatic limit reads [32]

$$\alpha_{\text{static}}(\omega) = \frac{V\omega_0^2}{\omega^2 - \omega_0^2 - i\omega\gamma} \tag{1}$$

[in CGS units, with $\omega$ the angular frequency, $\omega_0$ the particle resonance, $\gamma$ an Ohmic damping rate, and $V$ an (effective) particle volume], in the limit in which the response is locally approximated by a single resonance [43]. One must include radiation damping [30,32] to turn this polarizability into its dynamic form, which is required to build a self-consistent electrodynamic theory with a correct energy balance. For a particle in free-space, the dynamic polarizability reads

$$\frac{1}{\alpha} = \frac{1}{\alpha_{\text{static}}} - i\frac{2}{3}k^3 \tag{2}$$

(with $k = n\omega/c$). However, our case is somewhat different, since the particles are located inside a dielectric layered system which affects both the radiation damping correction, as well as redshifts the resonance frequency. In the following, we use the model given in Eqs. (1) and (2), and fit the plasmonic resonance model to our full wave simulations of a single inclusion in the dielectric stratified system (discussed further below). This fit yields a resonance frequency $\lambda_0 = 334 \times 10^{-9} + 3.6 \times 2r[m]$ and a damping rate $\gamma = 0.05\omega_0$, where $\omega_0 = 2\pi c/\lambda_0$, $k = 2\pi\sqrt{\epsilon_2}/\lambda_0$. It turns out that, while in rigorous terms the radiation damping in Eq. (2) should be corrected using the imaginary part of the Green's function at the location of the particle [34], it is a fair approximation to simply use Eq. (2) since the Ohmic damping in the particles dominates compared with the radiation loss, and its modification is also partially being taken into account by the fitting. Using this model, we can use a fitted analytical expression for the polarizability of the particles, which yields a very good approximation to the scattering cross section we obtain from full wave simulations in the diameter range 40–110 nm. As particles used in experiments are flat in the $z$ direction (30 nm height, versus 100 nm diameter typically), we constrain the particle polarizability to the $xy$ plane, meaning that dipole moments can only be excited in-plane.

The array is periodic by translation over $d$ in both the $x$ and $y$ directions, and thereby we can assume that the induced dipole moments assume a Bloch form $\mathbf{p}_{mn} = \mathbf{p}_{00}e^{id(nk_x+mk_y)}$, where $m,n$ are the particle indices and $(k_x,k_y)$ is the wave vector of the excited collective plasmonic mode parallel to the layers. For a lattice driven by an incident field of the form $\mathbf{E}_{\text{in}}e^{id(nk_x+mk_y)}$, the induced dipole moments are given by

$$\mathbf{p}_{00} = \alpha\left[\mathbf{E}_{\text{in}} + \sum_{n,m\neq 0,0} \mathbf{G}(\mathbf{r}_{00},\mathbf{r}_{mn})\mathbf{p}_{mn}\right]$$

or equivalently $\mathbf{p}_{00} = \frac{1}{\alpha^{-1}-\mathbf{C}}\mathbf{E}_{\text{in}}$ with

$$\mathbf{C} = \sum_{n,m\neq 0,0} \mathbf{G}(\mathbf{r}_{00},\mathbf{r}_{mn})e^{id(nk_x+mk_y)}.$$

Here the term $\mathbf{C}$ accounts for all dipole-dipole interactions and is also known as lattice sum [31–33,37–42]. The dyadic Green function $\mathbf{G}$ accounts for the full physics of the stratified system, meaning that it includes the TE and TM guided mode that the assumed slab supports, plus the continuous spectrum that accounts for radiation into the substrate and superstrate.

From this starting point, we can make several simplifications. The second order Bragg resonance on which lasing occurs at the $\Gamma$ point $(k_x,k_y) = (0,0)$ takes place in the two orthogonal directions parallel to the lattice primitive vectors [diffraction by lattice vectors $2\pi/d(\pm 1,0)$ and $2\pi/d(0,\pm 1)$]. Given the symmetry, without loss of generality we can analyze the $k_x = 0$ slice of the dispersion relation (propagation direction is $\hat{y}$), in which case the dipole polarization is along $\hat{x}$. Hence, the modal matrix problem reduces to the simplified scalar equation

$$\Delta(\omega,k_x,k_y) \equiv \alpha(\omega)^{-1} - C(\omega,k_x,k_y) = 0, \tag{3a}$$

$$C(\omega,k_x,k_y) = {\sum}' G_{xx}(\omega,\mathbf{r}_{00},\mathbf{r}_{mn})e^{id(mk_x+nk_y)}. \tag{3b}$$

In Eq. (3b), the symbol $\sum'$ denotes summation over all indices except $(m,n) = (0,0)$, and $G_{xx}$ is the $xx$ component (the $\hat{x}$ component of the electric field due to a $\hat{x}$ polarized dipole) of the electric Green's function tensor in the three-layer dielectric medium host.

Taking the full spectral content of the Green's function into account in the infinite summation in Eq. (3b) is numerically challenging, as the Green function in a stratified medium is generally expressed in angular spectrum representation as a parallel wave vector integral that includes guided modes as poles on top of a radiation continuum. We expect the Green function to be dominated by its poles on the basis of physical considerations: First, the distance between the particles corresponds to Bragg resonance at the TE mode, and second the particles strongly overlap with the TE waveguide mode as a consequence of their position in the slab, and their anisotropic, flat, geometry. Since the TE and TM modes of the slab (in absence of particles) are very close in dispersion, we expect significant TE-TM coupling. On this basis, we employ the assumption that we can neglect any continuous spectrum contribution to the Green's function, yet need to retain the TE and TM guided mode contribution to the Green function. Based on these considerations, we replace the full Green's function $G_{xx}$ with its modal part $G^m_{xx}$ including both TE and TM mode contributions, i.e., $G^m_{xx} = G^{\text{TE}}_{xx} + G^{\text{TM}}_{xx}$, where the TE and TM contributions are separately given by

$$G^{\text{TE}}_{xx} = 2A_{\text{TE}}\left[H_0^{(1)}(k_{\text{TE}}\rho) + \frac{\partial^2_{x'}H_0^{(1)}(k_{\text{TE}}\rho)}{(k_{\text{TE}})^2}\right], \tag{4a}$$

$$G^{\text{TM}}_{xx} = -2A_{\text{TM}}\left[\frac{\partial^2_{x'}H_0^{(1)}(k_{\text{TM}}\rho)}{k^2_{\text{TM}}}\right], \tag{4b}$$

where $\rho = \sqrt{(x-x')^2+(y-y')^2}$, and $k_{\text{TE}}$,$k_{\text{TM}}$ are the wave numbers in the transverse direction of the guided slab mode in the absence of the array, given by a solution of the corresponding mode transcendental equation [22]. The amplitudes $A_{\text{TE}}, A_{\text{TM}}$ are given by

$$A_X = \frac{k_0^3}{4\pi\epsilon_0}\frac{i}{2\eta_0}2\pi\xi_X g(z,z,\xi_X), \quad X = \text{TE, TM}, \tag{5}$$

where $\xi_X = k_X/k_0$, and $g$ is the 1D Green's function given in Appendix A. The infinite summation in Eq. (3) is slowly converging due to the inverse square root dependence of the Hankel function with respect to its argument. However, the convergence can be significantly accelerated applying the Ewald summation technique, adapted to the problem at hand (Appendix B).

Solution of Eq. (3) provides the complex-valued dispersion of the collective plasmonic excitation of the array in absence of gain. The lasing process in the structure is expected to build up in the regions of the frequency–wave number plane where the imaginary part of the complex wave number is minimal. To observe lasing, radiation must also couple out of the waveguide. Focusing on x-polarized excitation, the dipolar moment $p_{00}$ due to an impinging x-polarized plane wave with amplitude $E_0$ at $\omega$ with $(0,k_y)$ is given by $p_{00} = E_0/\Delta(\omega,0,k_y)$. By reciprocity, the radiated field due to a dipole strength $p_{00}$ at $\omega$ and (real) $(0,k_y)$ can be calculated from the reverse problem, i.e., from the induced dipole strength $p_{00}$ induced by an incident plane wave of given strength $E_0$, incident at $\omega$ with $(0,k_y)$. Therefore, the quantity $1/\Delta(\omega,0,k_y)$ essentially indicates the coupling between x-polarized induced dipoles and x-polarized far-field radiation with $k_{||} = k_y$. In the following section, based on this analytical model, we explore how the interplay of these two resonances controls the lasing mechanism in the lattice.

## III. THEORETICAL PREDICTION OF THE LASING CONDITIONS

Figure 2 shows the coupling efficiency between the excited dipolar moments and far-field radiation in a relatively wide frequency region around the TE Bragg resonance frequencies as grayscale where, black (white) represents poor (strong) radiation. Figures 2(b)–2(d) correspond to three distinct cases of interest, $\lambda_B^{\text{TE}} < \lambda_{\text{LSPR}}$, $\lambda_B^{\text{TE}} \approx \lambda_{\text{LSPR}}$, and $\lambda_B^{\text{TE}} > \lambda_{\text{LSPR}}$, respectively, where $\lambda_{\text{LSPR}}$ is the wavelength of the plasmonic particle resonance frequency, and $\lambda_B^{\text{TE}}$ is the free-space wavelength at which the second order TE mode Bragg resonance takes place. The salient feature is an anticrossing at $k_x = k_y = 0$ and $\omega$ around $3.1 \times 10^{15}$ s$^{-1}$ that involves four bands. These originate from the folded free-photon dispersion [Fig. 2(a)] that generates two linear bands [dispersion $k_y = n_{\text{TE}}\omega/c$ diffracted by $2\pi/d(0,\pm 1)$], and two parabolas [diffracted by $2\pi/d(\pm 1,0)$]. While in the case of significant red and blue detuning from the plasmon resonance (tuned by particle size) the photon dispersion is recognizable in the coupling efficiency $1/\Delta$ as narrow features close to the free-photon dispersion, for the on-resonance case, the dispersion is qualitatively different. In Figs. 2(e)–2(g) we zoom in at the frequency of the TE Bragg condition and plot the coupling efficiency (grayscale map) together with the complex dispersion of the collective

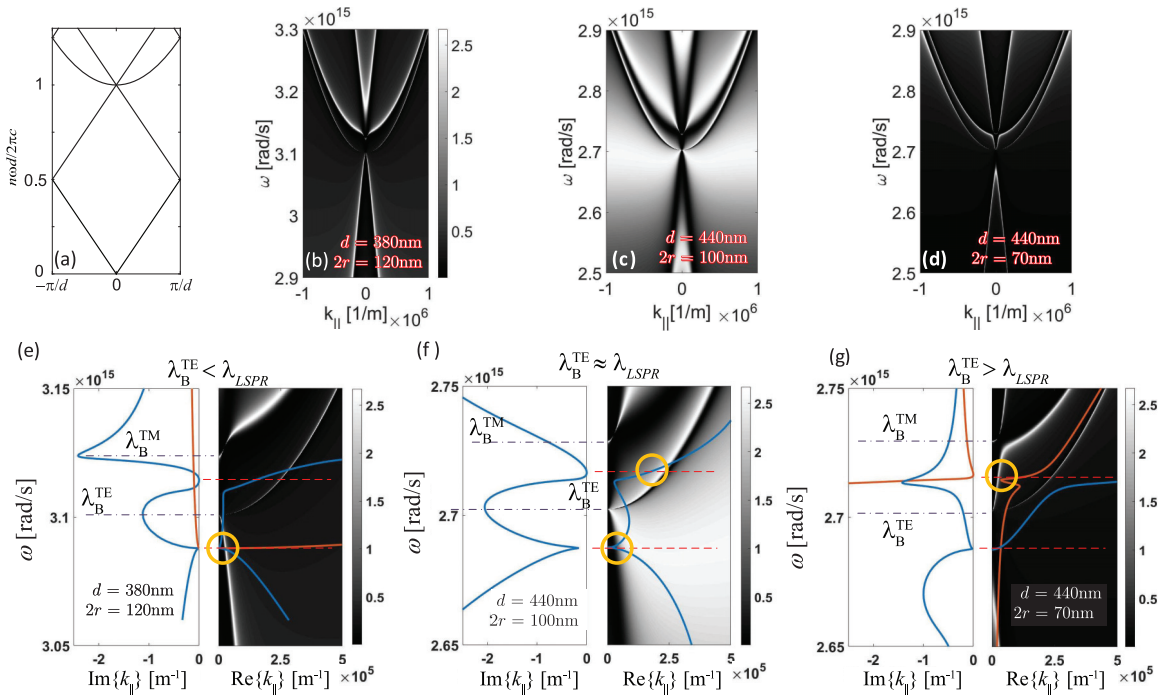


FIG. 2. (a) Sketch of the free-photon approximation to the dispersion relation between $k_y$ on the $x$ axis, and dimensionless frequency $n\omega d/2\pi c$, where $d$ is the lattice pitch and $n$ is the mode index. The dispersion relation folds back by diffraction at $2\pi/d(0, \pm 1)$ $[2\pi/d(\pm 1,0)]$ to give the lines (parabolas) crossing at $ky = 0$ (second order Bragg diffraction). (b)–(d) Coupling efficiency between $x$-polarized dipolar excitation and $x$-polarized far field for incidence in the $k_x$ zero plane (varying real $\omega$ and $k_y$). (a) $\lambda_B^{\mathrm{TE}} < \lambda_{\mathrm{LSPR}}$, (b) $\lambda_B^{\mathrm{TE}} \approx \lambda_{\mathrm{LSPR}}$, and (c) $\lambda_B^{\mathrm{TE}} > \lambda_{\mathrm{LSPR}}$. (e)–(g) The left panels show the dispersion of the imaginary part of $k_y$, while curves in the right-hand panels show the corresponding real part of the dispersion relation (blue and brown curves indicating different dispersion branches). The background grayscale shows the efficiency of coupling taken from (b)–(e). We expect that lasing is observed at a minimum of Im$k_y$ (indicated by red dashed lines) and simultaneously good outcoupling (conditions marked by circles). For reference in the left panels we indicate with black dashed lines the free-photon Bragg conditions for the TE and TM waveguide mode. (e)–(g) The same parameters as (b)–(d), meaning that they correspond to $\lambda_B^{\mathrm{TE}} < \lambda_{\mathrm{LSPR}}$ ($\lambda_B^{\mathrm{TE}} \approx \lambda_{\mathrm{LSPR}}$ and $\lambda_B^{\mathrm{TE}} > \lambda_{\mathrm{LSPR}}$).

plasmonic excitation, obtained as a solution of Eq. (3). This figure allows us to predict at which frequencies lasing is expected.

The curves (blue only or blue and brown) in each panel represent the relevant parts of the complex dispersion. In the left (right) side of each panel, we show the dispersion of the imaginary (real) part of $k_{||}$. Additional dispersion branches with much higher imaginary part are not shown, since we focus only on branches with an imaginary part close to zero that can contribute to lasing. For all three detuning scenarios considered, there are two frequencies for which the imaginary part of $k_{||}$ has a minimum. If only a single waveguide mode would contribute (e.g., TE only), only a single minimum would be expected, as one would expect one of the two stop gap edges to correspond to strong overlap (large loss), and one with weak overlap (low loss), of the corresponding Bloch mode with the particles. The fact that two minima occur is hence a sign of TE-TM coupling. While each minimum indicates a distributed resonance for which field amplification is expected when gain is added, observing clear laser output also requires efficient outcoupling. In other words, we now focus on simultaneously finding a frequency corresponding to minimum of Im$\{k_{||}\}$, and at the same time significant outcoupling as indicated by the grayscale colormaps on the right-hand side of each panel in Figs. 2(e)–2(g) (for Re$\{k_{||}\}$ near zero).

In the first scenario, shown in Fig. 2(e), $\lambda_B^{\mathrm{TE}} < \lambda_{\mathrm{LSPR}}$ is the only point for which we have a simultaneously low imaginary part of $k_{||}$ and significant coupling efficiency is at a frequency just above the kinematic TE Bragg condition (dashed line). In the opposite-detuning case, Fig. 2(g), $\lambda_B^{\mathrm{TE}} > \lambda_{\mathrm{LSPR}}$, the only point with low imaginary part of $k_{||}$ and simultaneously good outcoupling is below the kinematic TE Bragg condition. Finally, in the case in which particle resonance and lasing condition are tuned close to each other [Fig. 2(f), $\lambda_B^{\mathrm{TE}} = \lambda_{\mathrm{LSPR}}$], there are two points, one above and one below the TE Bragg condition, where this condition is satisfied. These results hence predict that for plasmon resonance and Bragg condition detuned from each other, one expects a distinct splitting in the dispersion relation, with lasing occurring always on the stop gap edge that is close to the plasmon resonance. For the intermediate case, both stop gap edges would lase. We further note that the proximity of the imaginary part of $k_{||}$ to the zero axis, and the brightness of the grayscale images representing coupling strength to radiation, are expected to relate to the lasing mode loss (and hence, required threshold) and lasing outcoupling efficiency. In the following, we discuss a campaign of experiments analyzing plasmonic arrays satisfying the three detuning conditions outlined in Fig. 2. Sections IV and V report on methods, while measured band structure results as a function of the detuning between Bragg condition and

plasmon resonance are discussed in Sec. VI and compared to the point dipole model in Sec. VII.

## IV. SAMPLE GEOMETRY, SETUP, AND CHARACTERIZATION OF THE GAIN MEDIUM

We fabricated silver particle arrays using electron beam lithography on ZEP resist, thermal evaporation of silver, and lift-off, on standard glass coverslips (Menzel, borosilicate). The square lattices are embedded in SU8. We study cylindrical particles with varying diameter (about 60 to 120 nm), and a height of about 30 nm. Since previously we established [20] that only silver gives advantageous results for plasmon lasers, owing to the much higher loss in other metals, this study focuses on silver. The dye-doped SU8 film of about 450 nm thickness is prepared by spin coating from a solution that is prepared by mixing equal parts of SU8-2005 (SU8 in cyclopentanone, 45% solids, Microchem) and cyclopentanone in which the dye is mixed. As gain medium we have used two systems. On one hand, with Rh6G as dye (5 mM in cyclopentanone), we can achieve gain near 590 nm. This requires small pitches, between 360 and 400 nm, and gives access to cases with particles red detuned from the gain medium. With a gain medium at 700 nm, and concomitantly larger lattice pitch of 460 nm, we can access blue detunings. To obtain a gain medium in this range that we can actually pump with our pump laser at 532 nm, we use a pair of dyes, namely 5 mM of Rh6G that absorbs the pump light, and acts as donor for Förster energy transfer to Rh700 which provides the gain, and which we have included at 0, 0.5, 3, 5, and 10 mM concentration. If one assumes that after spin coating all material except the cyclopentanone remains, dye concentrations in the film are approximately 2.2 times the nominal dye concentrations in solution. By ellipsometry we verified that the dye doped films have a refractive index of around 1.60, resulting in a single TE and a single TM mode that both have an effective index of about 1.55. We note that as the particle diameter is changed to control detuning, this changes the scattering strength at the lasing condition *both* because there is simply more polarizable matter per particle *and* because the resonance shifts.

We collect fluorescence emission that is resolved in frequency and parallel wave vector using the setup presented in Ref. [20] in which the sample is placed on an inverted optical microscope equipped with a 100× Nikon objective (Plan Apo NA = 1.45). We excited a 40 $\mu$m spot using 532 nm light offered in a 0.5 ns pulse with energy per pulse controlled in the range 0–20 nJ via an acousto-optical modulator. We also performed spectroscopy and fluorescence lifetime measurements on dye-doped films without plasmon particles to calibrate the dye system. To this end we used the fluorescence lifetime and spectroscopy setup presented in Ref. [44].

## V. SPECTROSCOPY OF CONSTITUENTS AND FRET

Figure 3 shows reference results for the gain medium composed of the FRET pair Rh6G and Rh700. Using samples without plasmonic particles, and low excitation amplitude, we measured emission spectra at fixed Rh6G concentration, and various Rh700 concentrations. Emission at the short wavelength end is clipped by a 540 nm longpass filter. Evidently the strong Rh6G emission band (550 to 620 nm) rapidly decreases in intensity as Rh700 is mixed into the film, while at the same time strong emission of the Rh700 dye (650 to 750 nm band) arises. At a one-to-one ratio (where the nominal dye concentrations prior to mixing with SU8 is 5 mM) the Rh6G emission has almost completely vanished. For larger concentration of Rh700, the Rh700 emission decreases, and redshifts. The disappearance of Rh6G emission and the appearance of Rh700 fluorescence, that is poorly pumped by 532 nm directly, is commensurate with Förster resonance energy transfer (FRET). As usual [45] we define the energy transfer efficiency as $E = 1 - F_{DA}/F_D$, where $F_D$ is the integrated (detector-corrected) spectral intensity of the donor-only sample, while $F_{DA}$ is the integrated spectral intensity of the acceptor. Figure 3(c) shows the energy transfer efficiency deduced from the data in (b) as a function of the nominal concentration (symbols) alongside the prediction [45–47]

$$E = -\sqrt{\pi}\gamma e^{\gamma^2}(1 - \mathrm{erf}\gamma)$$

that is appropriate for FRET in 3D homogeneous media. This expression depends only the dimensionless concentration $C/C_0$ via the parameter

$$\gamma = \frac{\Gamma(1/2)}{2}\frac{C}{C_0} \quad \text{with} \quad C_0 = \left(\frac{4}{\pi}R_0^3\right)^{-1},$$

where $\Gamma$ represents the Gamma function. We obtain a reasonable fit to the data for a critical concentration $C_0 = 0.9$ mM. Correcting for the difference between nominal concentrations *before* spin coating this result implies $C_0 = 2.2 \times 0.9$ mM *in* the SU8, which in turn translates to a Förster radius of about $R_0 = 5.5$ nm. Since this is on par with expected Förster radii [45], we conclude that the concentration dependence of spectra is consistent with FRET.

As an independent check, we also measured fluorescence decay traces of the donor emission. If energy transfer is due to FRET, decays should be given by [46]

$$I_D(t) = I_0 \exp\left[-t/\tau_D - 2\gamma(t/\tau_D)^{1/2}\right], \tag{6}$$

where $\tau_D$ is the donor decay time. Figure 3(d) shows measured decay traces at various concentrations alongside the prediction Eq. (6) convoluted with the instrument response function of our setup. We note that for this comparison we only adjust the overall scaling $I_0$, but adjust neither $\tau_D = 3.4$ ns, which is taken from a donor-only measurement, nor $\gamma$, which is taken from the spectral data. We note excellent correspondence, especially given that no parameter except overall scaling was adjusted. We identify the one-to-one 5 mM sample as most suited for our gain measurements as it provides strong Rh700 emission by FRET from Rh6G pumped by our 532 nm pump laser. From here onwards, in this paper we focus on samples with this gain medium, referring to them simply as "Rh700 samples."

It should be noted that in this paper we will not deeply discuss any *above*-threshold data, instead focusing on answering which mode reaches threshold (first) depending on the detuning between plasmon and Bragg condition. In order to

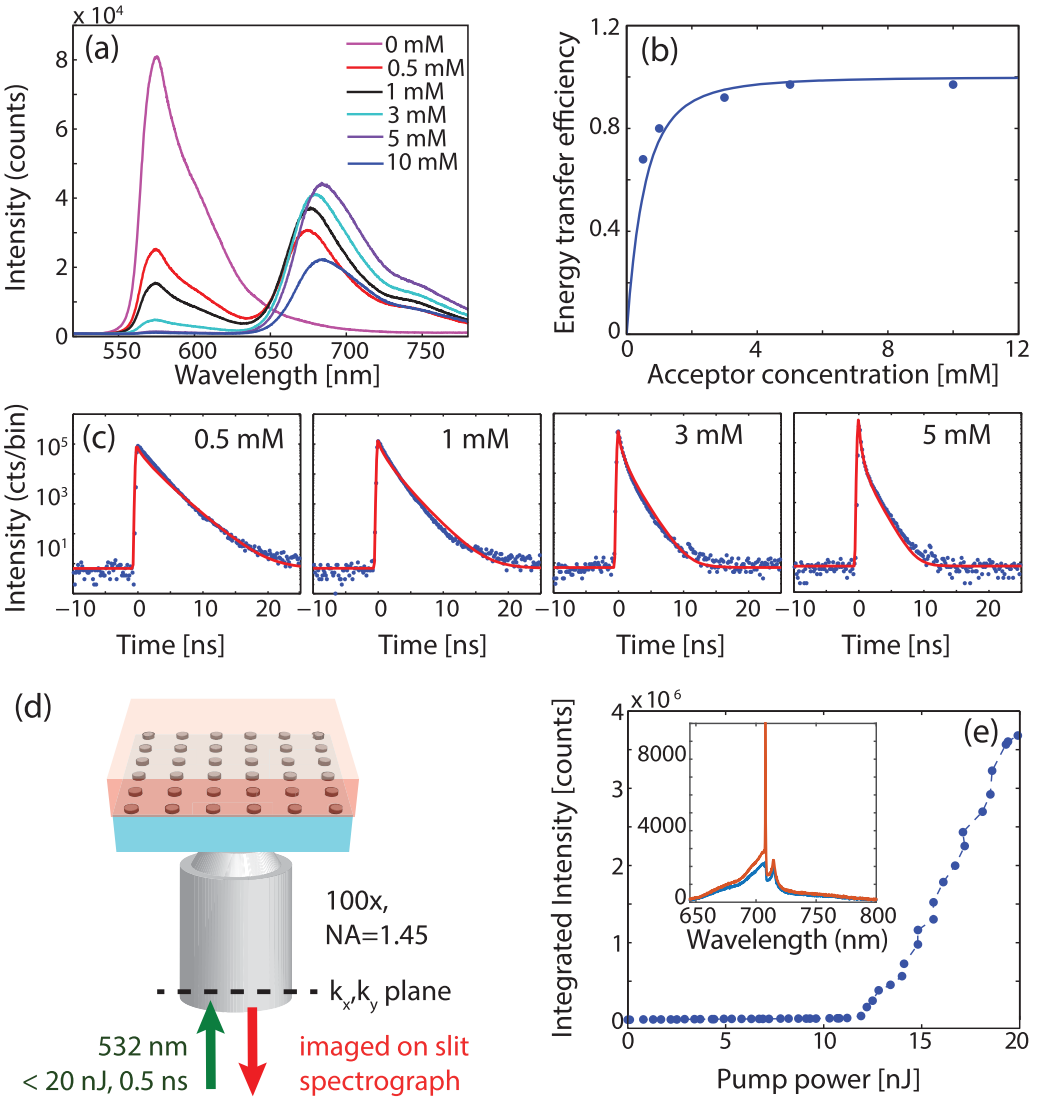


FIG. 3. (a) Emission spectra of dye mixtures under weak pumping. Here the concentration of Rh6G is fixed to 5 mM and the concentrations given in the figure represent Rh700 concentrations. (b) FRET efficiency curve from spectral integrals. The horizontal axis represents the concentration of Rh700, and the vertical axis represents energy transfer efficiency from the donor to the acceptor. (c) Lifetime traces for four concentrations (0.5, 1, 3, and 5 mM) of Rh700. The solid curves plotted through the data points are FRET theory where no adjustable parameter is used except a vertical scaling. (d) Sketch of the lasing setup consisting of a inverted fluorescence microscope used in back focal plane spectral imaging mode. (e) Spectra (inset) at pump powers just below (10 nJ, blue curve) and just above (15 nJ, orange curve), considering only a narrow band of wave vectors around $k_y = 0$. Note the stop gap and lasing on the blue edge of the stop gap. The intensity of the lasing peak shows distinct threshold behavior.

show that lasing does occur (for all the samples we report on), Fig. 3 shows an exemplary result for a sample with particle size $2r = 74$ nm in diameter and pitch of 460 nm, lasing at 710 nm, using the Rh6G:Rh700 dye mixture as gain medium. The spectra are obtained using the inverted fluorescence microscope in Fourier imaging mode [Fig. 3(d)]. At pump powers below about 12 nJ, the spectrum [Fig. 3(e), obtained by integrating only a narrow band of emission directions around $k_y = 0$] is similar to that on substrates with no particles, except for the appearance of a shallow gap near 715 nm. At the blue edge of this gap a narrow lasing peak appears for pump powers above 12 nJ. Tracing the intensity in a 5 nm wide spectral bin around the narrow lasing peak shows clear threshold behavior [20].

## VI. BAND DIAGRAMS

Figure 4 shows measured $\omega$,$k$ diagrams of fluorescence below threshold. The measurements generically display two linear bands, as well as the expected parabolic feature, with a distinct anticrossing centered around $2.63 \times 10^{15}$ s$^{-1}$ (715 nm, in accord with 1.55$d$). The most notable feature in Fig. 4 that is distinct from the free-photon folded dispersion relation sketched in Fig. 2(a) is that the two parabolic bands are not degenerate but distinctly split. Such a splitting is also observable in the calculated dispersion for the point dipole model. In particular, Figs. 2(d) and 2(g) corresponds to a particle size/pitch combination that can be compared with the data in Fig. 4(d), where the reader is admonished that the data

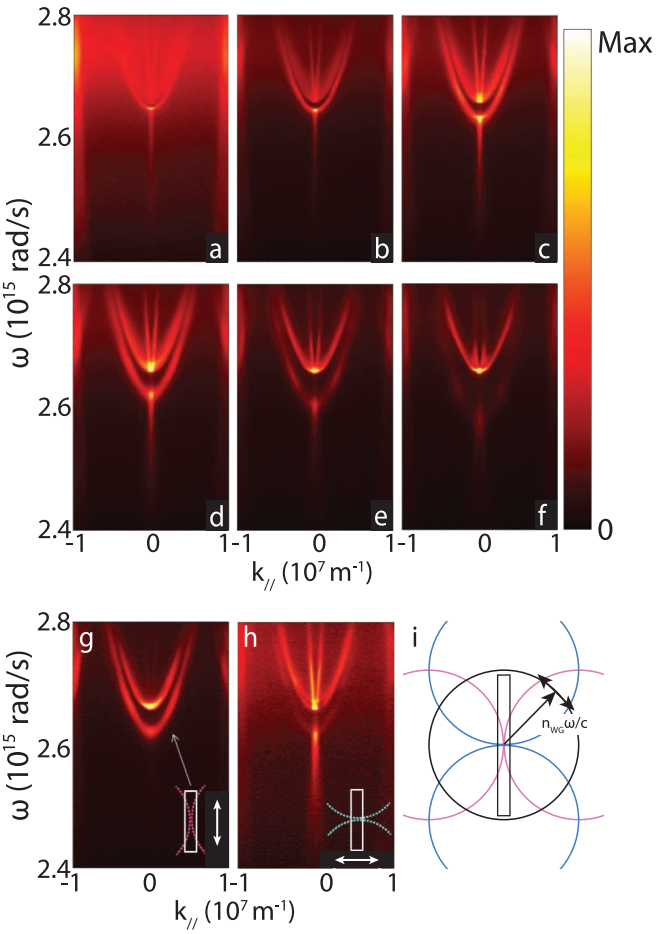


FIG. 4. Fluorescence (pumping below threshold) mapped in $\omega$-$k$ space as function of plasmon particle diameter, where the diameter varies from 53,61,74,82,86, to $95 \pm 5$ nm for (a)–(f), for samples with pitch $d = 460$ nm, using the Rh6G:Rh700 dye mixture, taken below threshold. Maxima are 5350, 8600, 11 650, 14 300, 25 200, and 27 950 counts/$\mu$J/shot, respectively. Note how the stop gap increase in size. (g) and (h) Polarization-resolved dispersion measurements for a particle diameter of 86 nm, taking polarization along and perpendicular to the spectrometer slit. (i) Sketch of parallel momentum space. At a fixed frequency $\omega$ (here chosen at second order Bragg diffraction), the slab waveguide mode appears as a circle of radius $n_{\mathrm{WG}}\omega/c$ centered at the origin (black), and due to diffraction by the lattice repeated every reciprocal lattice vector $2\pi/d(m,n)$ (color coded). For the TE waveguide mode, the electric field polarization is in-plane, normal to the momentum. The slit (rectangle) maps a slice of momentum space. In (g) and (h) the color bar maximum is at 5500 (2400) counts per $\mu$J of pump power.

extends over a wider frequency and wave number scale. In addition, the linear bands also show a stop gap, with band edges coincident with the minima of the parabola. This stop gap corresponds to the narrow gap visible also in Fig. 3(e) (inset) around 715 nm, at the blue edge of which lasing occurs once threshold is exceeded.

Fluorescence in momentum space is expected to show distinct structure tracing out features close to the waveguide-array dispersion [10,20], commensurate with the predictions that the outcoupling efficiency of the excited lattice will depend on frequency and angle [see maps of $1/\Delta(\omega,k_y)$ in Figs. 2(b)–2(d)]. Figures 4(a)–4(f) show the progression of the measured band structure as we increase particle size. Clearly the band structure stays qualitatively identical up to a particle size of 86 nm diameter, however, with a distinct increase in stop gap width. For particles above 95 nm in diameter, the band structure develops a qualitatively different appearance, both in terms of avoided crossing geometry, and in terms of the widths of the various bands. This is the regime where particles and lasing condition come in resonance, whereas for smaller diameters, the particles are blueshifted with respected to the Bragg condition that is set by the lattice.

The polymer slab supports two modes, the fundamental TE and fundamental TM mode, as reported in Figs. 1(c) and 1(d). According to our modeling both participate in setting the geometry of the anticrossing in Fig. 2, although outcoupling is predominantly through the TE waveguide. To verify this assertion we collected data on a series of samples using a linear polarizer in front of the spectrometer slit. To understand the measurement, we refer to a sketch of the repeated zone scheme dispersion that is projected on the spectrometer entrance plane [Fig. 4(i)]. Fluorescence is expected to dominantly be emitted into the waveguide mode. Since back focal plane imaging directly maps $\mathbf{k}_{||}/k_0$, this would appear on our detector as a ring that is $n_{\mathrm{TE,TM}} \approx 1.55$ times bigger then the free space light cone, if it were not for the fact that the objective clips the signal to its NA of 1.45. Bragg diffraction causes the dispersion to be replicated every reciprocal lattice vector $\mathbf{G} = 2\pi/d(m,n)$ (with $m,n$ integer), leading to a set of intersecting circles of radius $1.55k_0$ on the spectrometer entrance port [20]. In our measurement we only collect a slice along one axis (labeled $k_y$), spectrally dispersing the fluorescence from this slice over the other axis of our CCD camera. In such a measurement, the diffracted orders $\delta(|\mathbf{k}| - k_0 n_{\mathrm{mode}}) \pm 2\pi/d(0,1)$ appear as straight lines that intersect at $k_y = 0$ for the second order Bragg diffraction conditions. In contrast, the diffracted orders $\delta(|\mathbf{k}| - k_0 n_{\mathrm{WG}}) \pm 2\pi/d(1,0)$ appear as the two parabolas that have their minimum at the second order Bragg diffraction condition. If the dominant waveguide mode is TE (TM) polarized, i.e., tangential (radial) to the mode circles, this reasoning implies that the parabolic bands must be polarized along (crossed to) the slit, while the linear bands are polarized crossed to (along) the slit. Measurements of the band structure with a linear polarization analyzer along and across the slit are shown in Figs. 4(g) and 4(h) The observed behavior clearly indicates that the features we observe are strongly TE polarized. Indeed, the TE mode has a strong electric field component in the plane of the particles, along their main polarizability tensor axes. The TM mode mainly provides field along the sample normal. Through the small in-plane field, however, coupling between TE and TM polarized slab modes is possible via scattering at the particles. Especially the fact that the upper parabola remains visible in Fig. 4(h) indicates TE-TM mixing.

## VII. STOP GAP WIDTH

The measured band structures as a function of particle size indicate a strong dependence of gap width on particle scattering strength, or detuning. To quantify this relation, we extract the relative stop gap width ($\Delta\omega/\omega$) and plot it versus

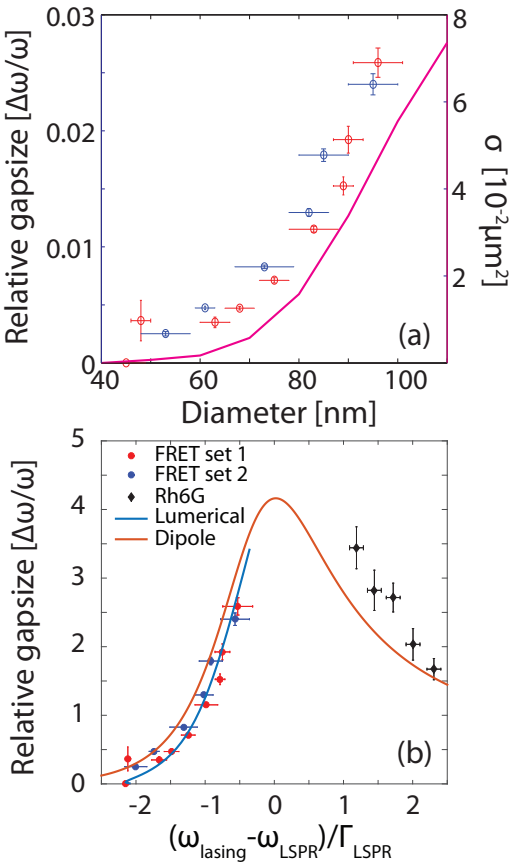


FIG. 5. (a) Relative stop gap width versus particle size. Red and blue points correspond to two distinct sample series. Error bars in particle size are from SEM measurements. The drawn line corresponds to the Lumerical-simulated extinction cross section. (b) Stop gap width versus normalized detuning between plasmon resonance and Bragg diffraction wavelength. Points in red and blue have been taken from Rh6G:Rh700 samples with large pitch (as in Fig. 4), while the black points at positive detuning are obtained using RH6G, with 110 nm particles and pitches from 360 to 400 nm [20]. The red line represents the scattering cross section expected in a dipole model, while in blue the cross section versus diameter from Lumerical calculations is shown, which is also plotted in (a).

particle size in Fig. 5(a). A direct relation between stop gap width and a scattering parameter such as cross section is not unexpected. For instance, in 3D dielectric photonic crystals of spheres the relative stop gap width is given by [48]

$$\frac{\Delta\omega}{\omega} = 4\pi\frac{\alpha}{V}, \tag{7}$$

where $\alpha$ stands for (electrostatic) polarizability (real and positive for dielectric spheres), and $V$ for the unit cell volume. At first sight it stands to reason that a similar relation holds in 2D plasmonic systems. However, in the plasmonic case the physics is richer, since $\alpha$ is a complex quantity, while stop gap widths must obviously be real and positive. There is no currently available theory that reports the equivalent of Eq. (7) for stop gap width in terms of scattering parameters of plasmon particles.

To bring out the dependence of stop gap width on scattering strength more clearly, we construct a "master diagram" that plots the data obtained here with the Rh6G-Rh700 FRET pair, and data obtained earlier with just Rh6G [20] as a function of a normalized frequency detuning parameter. We use the detuning between particle plasmon and lasing wavelength $\omega_{\mathrm{LSPR}} - \omega_{\mathrm{lasing}}$, normalized to the bandwidth of the plasmon resonance (FWHM $\Gamma_{\mathrm{LSPR}}$). Note that this is the only apparent relevant linewidth to normalize to in our system. The relevant single-particle frequency and linewidth are obtained by fitting a Lorentzian to the simulated particle response (specifically, $\sigma_{\mathrm{scat}}\lambda^4 \propto |\alpha|^2$). The data in Fig. 4 taken with Rh700 as gain medium appear at negative detuning, while data taken with Rh6G correspond to positive detuning. We remind the reader that for the Rh700 data we kept lasing frequency $\omega_{\mathrm{lasing}}$ fixed (fixed pitch), while particle size tuned the plasmon resonance $\omega_{\mathrm{lasing}}$ onto the lasing condition. For positive detuning, data were taken with a fixed particle size of 110 nm, varying pitch from 360 to 400 nm.

The resulting stop gap width clearly drops when detuning in either direction away from zero detuning, however, in an asymmetric fashion. Stop gap widths are about three times higher for detuning to the blue of the resonance, then for equal detuning to the red of the resonance. Such an asymmetry could be expected, in the sense that even if one starts with a Lorentzian polarizability $\alpha(\omega)$ as in Eq. (1), the scattering response of a plasmon particle is asymmetric in frequency as a consequence of radiation damping [Eq. (2)]. This is highlighted by plotting (cf. Fig. 5) the scattering cross section

$$\sigma_{\mathrm{scatt}} = \frac{8\pi}{3}k^4|\alpha|^2$$

for an archetypical Lorentzian scatterer alongside the data [taking typical Ohmic damping for silver ($\gamma = 0.05\omega_0$) and a particle volume chosen to obtain a scattering cross section at 80% of the unitary limit ($3/2\pi\lambda^2$)]. The stop gap width correlates well with the scattering cross section which shows a similar asymmetry as the data. For reference, in blue the cross section from full-wave simulations for each particle size [Fig. 1(b)], taken at the stop gap center frequency, is reproduced. It should be noted that Fig. 5 reports no stop gap width for any sample at zero detuning, although near-zero detuning is achieved for $2r > 100$ nm. As discussed below, for these large scattering strengths, the band structure we measure cannot be trivially traced to the original four-band crossing in a coupled-mode/slightly perturbed free-photon picture, hampering a stop gap width assignment.

## VIII. BAND STRUCTURE TOPOLOGY VERSUS DETUNING

We now turn to discussing more detailed features of the measured dispersion relations beyond just stop gap width. Figure 6 shows three measured dispersion diagrams. Figure 6(a) shows a dispersion diagram taken from Ref. [20], obtained on a sample that has the lasing condition well to the blue of the localized surface plasmon resonance (Rh6G sample, $d = 380$ nm, 55 nm radius particle). Figure 6(c) shows a dispersion diagram for the converse case, i.e., with the lasing condition well to the red of the plasmon resonance [case (e), Fig. 4]. The panel in the middle, finally, corresponds to a case where the lasing condition is aligned to the plasmon

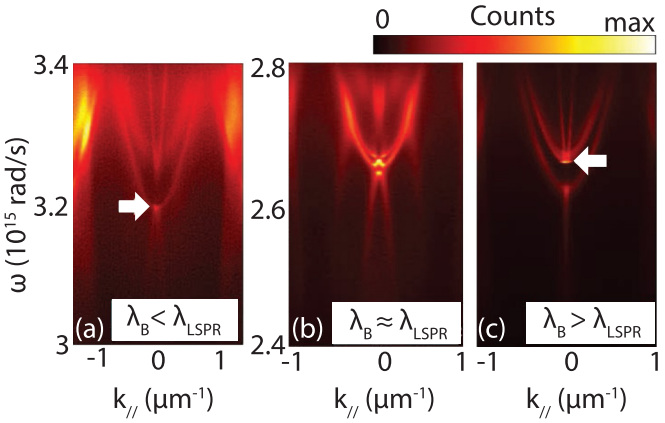


FIG. 6. Generic $\omega$-$k$ diagrams for three cases: lasing condition blue detuned, red detuned, and centered on the plasmon resonance [(a), (c), and (b)]. These concern (a) $d = 380, 2r = 55$ nm, (b) $d = 460, 2r = 129$ nm, and (c) $d = 460, 2r = 86$ nm. For (a) we used Rh6G only, while the other panels used the Rh6G:Rh700 FRET mixture. White arrows indicate the $\omega$-$k$ point on which system lases first.

resonance (Rh700 sample, particle diameter 129 nm). These three detuning cases correspond to the separation into blue detuning, zero detuning, and red detuning case that we also presented for our theory results in Fig. 2.

We note the following progression in the data. First, when the Bragg condition is well to the red of the localized surface plasmon resonance [negative detuning, Fig. 6(c)], the lower and upper parabola have their minima coincident with the maximum and minimum of the anticrossing linear dispersion relations, quite similar to nearly free-photon band structure predictions would yield [36,49]. Lasing in these samples always occurs on the upper band edge, consistent with the complex dispersion analysis in Fig. 2. The fact that the parabola and the anticrossing lines share a common gap is consistent with the scalar coupled mode theory for dielectric DFB lasers (adapted to metal hole array plasmon lasers by van Exter *et al.* [49, Fig. 4b]) in the limit that coupling by $\mathbf{G} = 2\pi/d(0, \pm 1)$ and $(\pm 1, 0)$ dominates, and $(\pm 1, \pm 1)$ scattering is weak. For the opposite-detuning case, i.e., Fig. 6(a) in which the Bragg condition occurs to the blue of the particle resonance (positive detuning), again two split parabola, and two anticrossing linear bands are retrieved, now with the upper parabola consistently very broad. For these samples lasing occurs on the lower stop gap edge instead of the upper stop gap edge, again commensurate with the complex-valued dispersion analysis reported in Fig. 2. Finally, when the particle plasmon and lasing condition coincide, i.e., Fig. 6(b), the band structure is markedly different. The minimum of the lower parabola is pushed below the frequency range of the measurement, and a set of additional features has appeared that cannot be trivially traced to the original four-band crossing in a coupled-mode/slightly perturbed free-photon picture [for which reason, the sample in Fig. 6(b) does not appear as a data point in Fig. 5]. Lasing occurs on both apparent band edges, with similar thresholds.

## IX. REAL SPACE COMSOL STUDY

Complementary to a wave vector space study that identifies which dispersion branches have low loss, yet good outcoupling, one can also perform a real space analysis that targets to understand what distinguishes the modes with large and low loss. A likely explanation carries over from coupled mode theory and the field of photonic crystals, where it is well known that gap edge modes are standing waves concentrated at different locations in the unit cell. For dielectric photonic crystals the band with the most energy density in the dielectric (air) corresponds to the the lower (upper) band edge, giving rise to the terminology of "dielectric (air) band." One can hypothesize that also in plasmonic crystals one band will reside at, and one band will reside away from, the plasmon particles. The energetic ordering, as well as the Ohmic loss, of these two bands could then be expected to flip when the sign of the scattering potential, i.e., polarizability $\alpha$ flips, which occurs as one goes from negative to positive detuning. In turn this would explain that opposite sign of detuning also implies a swap in the band edge that lases.

Since dipole models are not suited to obtain near fields, we consider a COMSOL 3D finite element simulation. As indices for the dielectric stack we take 1.46/1.65/1.0—although the actual glass we use is not quartz but fused silica ($n = 1.52$), and the SU8 index from ellipsometry is actually 1.60, not the data sheet value of 1.65. The reason for this choice is that it provides a larger separation between waveguide mode indices, and hence easier separation in the discussion, between waveguide modes, and plain diffraction into the glass. Figure 7(a) shows calculated lattice extinction alongside the single particle resonance in Fig. 7(b). As particles we assume silver disks of height 30 nm and diameter 100 nm. The single-particle extinction [Fig. 7(b)] shows a strong resonance at $\omega = 2.76 \times 10^{15}$ s$^{-1}$, equivalent to 680 nm light, comparable to the result in Fig. 3. Next, we implemented Bloch-Floquet boundary conditions to obtain the diffractive properties upon plane wave driving incident from the glass side. We studied two pitches, i.e., 500 and 370 nm, to meet the second order Bragg condition on either side of the resonance, and use slightly off-normal excitation (0.5° along $k_y$) to make sure that symmetry does not forbid coupling.

Figure 7(a) shows the transmission in a small frequency range around the diffractive coupling condition for both pitches. The curves present the following three features. First, the generally high transmission is dominated by a relative broad (though still narrow compared to the plasmon resonance) asymmetric minimum that has the appearance of a Fano line shape. Second, the spectra show two extremely narrow features. The frequency at which the two narrow features occur match very well with diffractive coupling to the TE and TM waveguide mode. We interpret the wide minimum, and the narrow TE feature as the relevant lower, and upper stop gap edge for the TE-like waveguide mode. This assignment is supported by examination of field cross cuts (see below). Note that for the large-pitch case $d = 500$ nm, the broad minimum occurs at a frequency *below* the narrow feature, while for the small-pitch case, the ordering is reversed. We examine the scattered fields (i.e., full field, minus the field that we calculate in absence of the particle) upon plane wave driving

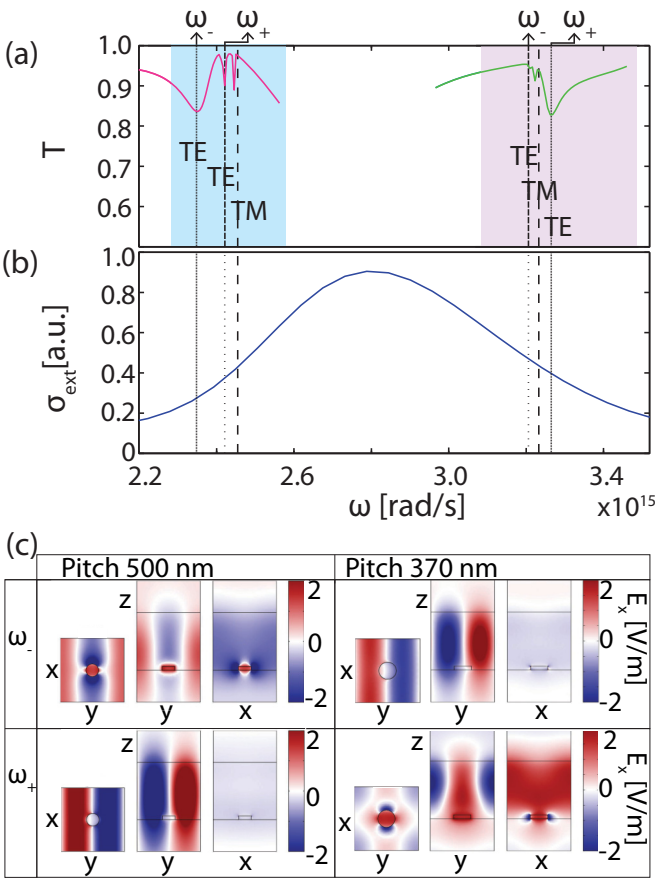


FIG. 7. The blue curve in (b) shows the extinction cross section for a single silver disk with a height of 30 nm and a diameter of 100 nm on a substrate with index $n = 1.46$, embedded in a waveguide with a refractive index of 1.65 and a thickness of 450 nm. (a) Transmission for an array of these particles with a pitch of 500 (pink) and 370 nm (green). The pink and blue areas represent the frequencies limited by $\omega = 2\pi c n_{\mathrm{mat}} d$ with $n_{\mathrm{mat}} = 1.65$ and 1.46 for both pitches that would correspond to grazing angle grating coupling into solid SU8, or the glass. The dotted lines show the frequencies for which the waveguide mode without particles has a TE and a TM mode, as indicated. We label the broad and narrow dip that are associated with the stop gap edges as $\omega_-$ and $\omega_+$ [near 2.4 ($3.25 \times 10^{15}$ s$^{-1}$) for pitches of 500 nm (370 nm)]. (c) Crosscuts in the $xy$ plane, $xz$ and $yz$ plane through one unit cell of a particle array for frequencies $\omega_-$ and $\omega_+$ indicated in (a), for pitches 500 and 370 nm as marked. Plotted is scattered field $E_x - E_{x,\mathrm{in}}$ along the 1 V/m $x$-oriented incident field.

at the center frequencies of the broad and narrow minima. Figure 7(c) shows the scattered field component $E_x$ that is along the incident polarization for both pitches, and for each pitch at the labeled lower and upper gap edge $\omega_\pm$. The vertical cuts show that the transverse field distributions are essentially the mode profile of a TE mode. At the frequency of the narrow feature [$\omega_+$ ($\omega_-$) for the large (small) pitch case], the scattered field has a nodal plane at the particle, and resides mainly away from it. Conversely, at the broad minimum in transmission, the associated field plot shows strong excitation of the particle. The COMSOL simulation hence corroborates the interpretation that lasing selects the stop gap edge that corresponds to the Bloch mode that forms a standing wave with energy density predominantly away from the particle, as this is the lowest-loss mode that still couples out. As one goes through resonance, the stop gap edge to which this standing wave corresponds is reversed, as the real part of the polarizability flips sign.

## X. CONCLUSIONS AND OUTLOOK

In summary, we have shown how the optical response of plasmonic scatterers affects the band diagram of a plasmon particle array embedded in a dye doped waveguide layer. By combining data for lasers with various particle sizes, pitches, and two gain media near 590 nm and FRET-based gain at 700 nm, we were able to systematically map the behavior of plasmon lattice lasers as a function of the detuning between particle resonance and lasing condition as set by the lattice periodicity. A main conclusion is that the stop gap width in the band structure of the plasmon lattice lasers is much larger than in dielectric distributed feedback lasers, and is essentially proportional to the particle scattering cross section. Commensurate with the complex lattice dispersion that we calculate from an electrodynamic coupled dipole model, the stop gap edge that gives rise to lasing is always the one closest to the particle resonance, and corresponds to the condition of a low loss Bloch mode that at the same time has nonzero outcoupling efficiency. While the strong scattering by plasmon particles couples TE and TM mode, the outcoupled light is of TE nature. When plasmon and lattice resonance are aligned, the band structure is particularly far from a nearly free-photon approximation, which is qualitatively correct only for lasing far to the red of the plasmon resonance.

We note that our work also provides pointers for further experiments and theory. Any theory must account at least for the scaling of stop gap with scattering strength, the qualitatively very different band structure at zero detuning, and for subtle features such as where the mode resides and what mode has least loss, depending on the choice of detuning. It is a surprisingly challenging problem to build a theory for this system. Coupled mode theory [36,49] would treat the particles as a weak perturbation, and is essentially valid only for small dielectric perturbations. Numerically the difficulties in extending it to plasmon particles are clear from the fact that Fourier modal, i.e., plane wave expansion, methods are very poorly convergent for plasmon particle gratings [20]. Coupled dipole theory as presented here can treat complex-valued dispersion relations at very large scattering strength, yet only provides partial insight into laser physics. A more refined treatment of near fields and of nonlinear dynamics of lasing above threshold is required to quantitatively account for loss, local pump and Purcell enhancements, the overlap of modes with the gain medium, and gain dynamics. Finite element treatment, finally accurate for near field, can include gain [29] and allows complicated unit cell geometries. However, although possible, this approach may be significantly more computationally demanding when extended to deal with *complex-valued* dispersion relations of decaying modes. Experiments that could guide these theoretical efforts would for instance include studying variations in particle material, or using core-shell geometries, to independently vary physical particle volume, loss, and scattering cross sections. Also we envision that using gain media of different spatial

distributions, be it arranged lithographically or by controlling the optical pump field [50], and gain media of different quantum efficiency, will allow us to unravel the role of near field enhancements. Finally, we note that our considerations likely also carry over to lasing structures that use surface lattice resonances, but no waveguide [17–19]. In the case of surface lattice resonances there is no waveguide, but lasing does occur at resonance crossings [17–19]. According to Rodriguez *et al.* [51], extinction spectra of such systems also can show gaps, with a width that depends on the tuning of local plasmon resonance and diffraction condition. In our system, evidently lasing occurs on a hybrid plasmonic-photonic mode where the waveguide helps us to optimize mode overlap with the scatterers, thereby aiding the opening of a stop gap that is wide.

## ACKNOWLEDGMENTS

We thank Marko Kamp for technical support with the experiment, and Alexei Halpin for a critical reading of the manuscript. This work is part of the research programme of the Netherlands Organisation for Scientific Research (NWO). This work was furthermore supported by NanoNextNL, a microtechnology and nanotechnology consortium of the Government of the Netherlands and 130 partners. A.A. was partially supported by a Visiting Professorship of the KNAW, the Royal Netherlands Academy of Arts and Sciences. Y.H. and A.A. were also supported by the Air Force Office of Scientific Research, the Welch Foundation with Grant No. F-1802, and the Simons Foundation.

## APPENDIX A: 1D GREEN'S FUNCTION

First we define normalized longitudinal wave numbers $\zeta_i^X = \sqrt{\epsilon_{ri} - \xi_X^2}$, with $X = \mathrm{TE/TM}$ and subject to the radiation condition $\mathrm{Im}\{\zeta_i^X\} \geqslant 0$. Then, the 1D Green's function used in Eq. (5) is given by

$$g(\omega,z,z') = \frac{1}{2}\frac{Z_2^X}{D_X}\left(e^{ik_z^X|z-z'|} + R_1^X e^{ik_z^X[2h-(z+z')]} + R_3^X e^{ik_z^X(z+z')} + R_1^X R_3^X e^{ik_z^X(2h-|z-z'|)}\right), \quad \text{(A1)}$$

where $h$ is the SU8 layer thickness and $k_z^X = k_0\zeta_2^X$, and

$$R_i^X = \frac{Z_i^X - Z_2^X}{Z_i^X + Z_2^X}, \quad i = 1,3,$$

$$Z_i^{\mathrm{TM}} = \eta_0\frac{\zeta_1^{\mathrm{TM}}}{\epsilon_{ri}}, \quad Z_i^{\mathrm{TE}} = \frac{\eta_0}{\zeta_i^{\mathrm{TE}}}, \quad i = 1,2,3,$$

and

$$D_X = \frac{d}{d\xi}\left(1 - R_1^X R_3^X e^{2ik_0\zeta_2^X h}\right)\Big|_{\xi_X = k_X/k_0}.$$

## APPENDIX B: EWALD SUMMATION

The convergence of the infinite summation in Eq. (3) can be significantly accelerated by using the Ewald summation technique [31–33,37–42]. First, we write

$$C(\omega,k_x,k_y) = 2A_{\mathrm{TE}}\left(S(k_{\mathrm{TE}}) + \frac{S_{xx}(k_{\mathrm{TE}})}{k_{\mathrm{TE}}^2}\right) - 2A_{\mathrm{TM}}\frac{S_{xx}(k_{\mathrm{TM}})}{k_{\mathrm{TM}}^2}, \quad \text{(B1)}$$

with $k_{\mathrm{TE}} = k_0\xi_{\mathrm{TE}}$, and $k_{\mathrm{TM}} = k_0\xi_{\mathrm{TM}}$, and

$$S(k) = \lim_{x'y'\to 0}{\sum}' H_0^{(1)}(kR_{mn})e^{id(mk_x+nk_y)}, \quad \text{(B2a)}$$

$$S_{xx}(k) = \partial_{x'x'}S(k), \quad \text{(B2b)}$$

where $R_{mn} = \sqrt{(x'-md)^2 + (y'-nd)^2}$. The primed summation sign in Eq. (B2a) is used to exclude the $(m,n) = (0,0)$ term from the infinite two-dimensional summation. The summation can also be written as

$$S(k) = \lim_{x'y'\to 0}{\sum} H_0^{(1)}(kR_{mn})e^{id(mk_x+nk_y)} - H_0^{(1)}(k\rho'),$$

where $\rho' = \sqrt{x'^2 + y'^2}$. The unprimed summation is used for infinite summation $(m,n) \in (-\infty,\infty) \times (-\infty,\infty)$. Next we replace the Hankel function by one of its integral representations

$$H_0^{(1)}(kR_{mn}) = -\frac{2i}{\pi}\int_0^\infty \frac{du}{u}e^{(k^2/4u^2 - R_{mn}^2u^2)}.$$

Note that since $R_{mn}^2 > 0$, and assuming that $k^2 > 0$, to formally guarantee convergence of the integral representation in Eq. (B3) we have to require that $u$ pass to infinity along the line $\arg u = -\pi/4$. However, once we use this representation and derive an alternative, rapidly converging representation for the summation, we may apply Cauchy theorem and calculate the required integrals along a more convenient path.

The semi-infinite integration path above is decomposed into two intervals, $0 \to E$ and $E \to \infty$, where $E$ is an arbitrarily chosen constant picked as a trade off between fast convergence of $S_1$ and $S_2$. We define

$$S_1 = {\sum} -\frac{2i}{\pi}\int_0^E \frac{du}{u}e^{(k^2/4u^2 - R_{mn}^2u^2)}e^{id(mk_x+nk_y)}, \quad \text{(B3a)}$$

$$S_2 = {\sum}' -\frac{2i}{\pi}\int_E^\infty \frac{du}{u}e^{(k^2/4u^2 - R_{mn}^2u^2)}e^{id(mk_x+nk_y)}, \quad \text{(B3b)}$$

$$C = \frac{2i}{\pi}\int_0^E \frac{du}{u}e^{(k^2/4u^2 - \rho'^2u^2)}, \quad \text{(B3c)}$$

such that $S = S_1 + S_2 + C$. Note that as long as $E \gg k/2$, the integration in the summands of $S_2$ yields a Gaussian decay of the summands with respect to the summation indexes hence the summation over this part of the integral convergence rapidly. Similarly, the integration required to calculate $C$ converge

rapidly. The only issue left is the slow convergence of $S_1$ which is similar to the poor convergence of the original series. In this case, however, we are able to apply Poisson summation to accelerate the convergence. We obtain

$$S_1 = \frac{4i}{d^2} \sum_{p,q} \frac{e^{k_{zpq}^2/4E^2}}{k_{zpq}^2}, \tag{B4}$$

where $\mathbf{k}_{\rho pq} = (k_x, k_y) - 2\pi/d(p,q)$, and $k_{zpq}^2 = k^2 - \mathbf{k}_{\rho pq} \cdot \mathbf{k}_{\rho pq}$, $p,q \in \mathcal{Z}^2$ ($\mathcal{Z}$ denotes the set of integers). The convergence of the summation for $S_1$ in its new representation is Gaussian, therefore, practically only a few terms are required.

Finally, we have $S_{xx} = S_{1xx} + S_{2xx} + C_{xx}$, where

$$S_{1xx} = -\frac{4i}{d^2} \sum_{p,q} \frac{e^{k_{zpq}^2/4E^2}}{k_{zpq}^2} \left(k_x - \frac{2\pi}{d} p\right)^2, \tag{B5a}$$

$$S_{2xx} = \sum{}' \frac{4i}{\pi} \int_E^\infty du(1 - 2m^2 d^2 u^2)u \times e^{\left(k^2/4u^2 - R_{mn}^2 u^2\right)} e^{id(mk_x + nk_y)}, \tag{B5b}$$

$$C_{xx} = -\frac{4i}{\pi} \int_0^E duue^{\left(k^2/4u^2 - \rho'^2 u^2\right)}. \tag{B5c}$$


[1] I. D. W. Samuel and G. A. Turnbull, Chem. Rev. **107**, 1272 (2007).
[2] G. Heliotis, R. D. Xia, G. A. Turnbull, P. Andrew, W. L. Barnes, I. D. W. Samuel, and D. D. C. Bradley, Adv. Funct. Mater. **14**, 91 (2004).
[3] G. A. Turnbull, P. Andrew, M. J. Jory, W. L. Barnes, and I. D. W. Samuel, Phys. Rev. B **64**, 125122 (2001).
[4] P. Del Carro, A. Camposeo, R. Stabile, E. Mele, L. Persano, R. Cingolani, and D. Pisignano, Appl. Phys. Lett. **89**, 201105 (2006).
[5] E. Mele, A. Camposeo, R. Stabile, P. Del Carro, F. Di Benedetto, L. Persano, R. Cingolani, and D. Pisignano, Appl. Phys. Lett **89**, 131109 (2006).
[6] S. A. Maier, *Plasmonics: Fundamentals and Applications* (Springer, Berlin, 2007).
[7] G. M. Akselrod, C. Argyropoulos, T. B. Hoang, C. Cirac, C. Fang, J. Huang, D. R. Smith, and M. H. Mikkelsen, Nat. Photon. **8**, 835 (2014).
[8] C. Belacel, B. Habert, F. Bigourdan, F. Marquier, J.-P. Hugonin, S. Michaelis de Vasconcellos, X. Lafosse, L. Coolen, C. Schwob, C. Javaux, B. Dubertret, J.-J. Greffet, P. Senellart, and A. Maitre, Nano Lett. **13**, 1516 (2013).
[9] E. J. R. Vesseur, F. J. G. de Abajo, and A. Polman, Phys. Rev. B **82**, 165419 (2010).
[10] S. Murai, M. A. Verschuuren, G. Lozano, G. Pirruccio, S. R. K. Rodriguez, and J. G. Rivas, Opt. Express **21**, 4250 (2013).
[11] G. Vecchi, V. Giannini, and J. G. Rivas, Phys. Rev. Lett. **102**, 146807 (2009).
[12] A. G. Nikitin, A. V. Kabashin, and H. Dallaporta, Opt. Express **20**, 27941 (2012).
[13] P. L. Stiles, J. A. Dieringer, N. C. Shah, and R. R. Van Duyne, Annu. Rev. Anal. Chem. **1**, 601 (2008).
[14] M. E. Stewart, C. R. Anderton, L. B. Thompson, J. Maria, S. K. Gray, J. A. Rogers, and R. G. Nuzzo, Chem. Rev. **108**, 494 (2008).
[15] J. N. Anker, W. P. Hall, O. Lyandres, N. C. Shah, J. Zhao, and R. P. Van Duyne, Nat. Mater. **7**, 442 (2008).
[16] G. Lozano, D. J. Louwers, S. R. K. Rodriguez, S. Murai, O. T. A. Jansen, M. A. Verschuuren, and J. G. Rivas, Light. Sci. Appl. **2**, e66 (2013).
[17] W. Zhou, M. Dridi, J. Y. Suh, C. H. Kim, D. T. Co, M. R. Wasielewski, G. C. Schatz, and T. W. Odom, Nat. Nanotechnol. **8**, 506 (2013).
[18] J. Y. Suh, C. H. Kim, W. Zhou, M. D. Huntington, D. T. Co, M. R. Wasielewski, and T. W. Odom, Nano Lett. **12**, 5769 (2012).
[19] A. Yang, T. B. Hoang, M. Dridi, C. Deeb, M. H. Mikkelsen, G. C. Schatz, and T. W. Odom, Nat. Commun. **6**, 6939 (2015).
[20] A. H. Schokker and A. F. Koenderink, Phys. Rev. B **90**, 155452 (2014).
[21] A. H. Schokker and A. F. Koenderink, ACS Photon. **2**, 1289 (2015).
[22] H. P. Urbach and G. L. J. A. Rikken, Phys. Rev. A **57**, 3913 (1998).
[23] M. J. Weber, *Handbook of Optical Constants of Materials* (CRC, Boca Raton, FL, 2003).
[24] L. Zhao, K. L. Kelly, and G. C. Schatz, J. Phys. Chem. B **107**, 7343 (2003).
[25] A. Bouhelier, R. Bachelot, J. Im, G. Wiederrecht, G. Lerondel, S. Kostcheev, and P. Royer, J. Phys. Chem. B **109**, 3195 (2005).
[26] M. Meier and A. Wokaun, Opt. Lett. **8**, 581 (1983).
[27] M. Dridi and G. C. Schatz, J. Opt. Soc. Am. B **30**, 2791 (2013).
[28] J.-P. Martikainen, T. K. Hakala, H. T. Rekola, and P. Törmä, J. Opt. **18**, 024006 (2016).
[29] J. Cuerda, F. Rüting, F. J. García-Vidal, and J. Bravo-Abad, Phys. Rev. B **91**, 041118 (2015).
[30] P. de Vries, D. V. van Coevorden, and A. Lagendijk, Rev. Mod. Phys. **70**, 447 (1998).
[31] F. Capolino, D. R. Jackson, D. R. Wilton, and L. B. Felsen, IEEE Trans. Antennas Propag. **55**, 1644 (2007).
[32] F. J. G. de Abajo, Rev. Mod. Phys. **79**, 1267 (2007).
[33] A. Kwadrin and A. F. Koenderink, Phys. Rev. B **89**, 045120 (2014).
[34] Y. Hadad and B. Z. Steinberg, *2010 URSI International Symposium on Electromagnetic Theory* (IEEE, Berlin, Germany, 2010), p. 680.
[35] D. Van Orden, Y. Fainman, and V. Lomakin, Opt. Lett. **34**, 422 (2010).
[36] H. Kogelnik and C. Shank, Appl. Phys. Lett. **18**, 152 (1971).
[37] S. Steshenko, F. Capolino, P. Alitalo, and S. Tretyakov, Phys. Rev. E **84**, 016607 (2011).
[38] P. Lunnemann, I. Sersic, and A. F. Koenderink, Phys. Rev. B **88**, 245109 (2013).
[39] A. L. Fructos, S. Campione, F. Capolino, and F. Mesa, J. Opt. Soc. Am. B **28**, 1446 (2011).
[40] K. Kambe, Z. Naturforsch., A: Astrophys., Phys. Phys. Chem. **23**, 1280 (1968).
[41] C. M. Linton, SIAM Rev. **52**, 630 (2010).
[42] Y. Mazor and B. Z. Steinberg, Phys. Rev. Lett. **112**, 153901 (2014).

[43] M. Agio and A. Alù, *Optical Antennas* (Cambridge University Press, Cambridge, 2013), p. 31.
[44] A. Mohtashami and A. F. Koenderink, New J. Phys. **15**, 043017 (2013).
[45] J. R. Lakowicz, *Principles of Fluorescence Spectroscopy* (Springer, Berlin, 2006).
[46] K. B. Eisenthal and S. Siegel, J. Chem. Phys. **41**, 652 (1964).
[47] T. Förster, Ann. Phys. **437**, 55 (1948).
[48] W. L. Vos, R. Sprik, A. van Blaaderen, A. Imhof, A. Lagendijk, and G. H. Wegdam, Phys. Rev. B **53**, 16231 (1997).
[49] M. P. van Exter, V. T. Tenner, F. van Beijnum, M. J. A. de Dood, P. J. van Veldhoven, E. J. Geluk, and G. W. 't Hooft, Opt. Express **21**, 27422 (2013).
[50] G. Pirruccio, M. Ramezani, S. R.-K. Rodriguez, and J. G. Rivas, Phys. Rev. Lett. **116**, 103002 (2016).
[51] S. R. K. Rodriguez, A. Abass, B. Maes, O. T. A. Janssen, G. Vecchi, and J. Gómez Rivas, Phys. Rev. X **1**, 021019 (2011).